Fusion of the MR Image to SPECT With Possible Correction for Partial Volume Effects

Piero Calvini, Anna Maria Massone, Flavio Mariano Nobili, and Guido Rodriguez

***Abstract*—Low spatial resolution and the related partial volume effects limit the diagnostic potential of brain single photon emission computed tomography (SPECT) imaging. As a possible remedy for this problem we propose a technique for the fusion of SPECT and MR images, which requires for a given patient the SPECT data and the T1-weighted MR image. Basically, after the reconstruction and coregistration steps, the high-frequency part of the MR, which would be unrecoverable by the set SPECT acquisition system + reconstruction algorithm, is extracted and added to the SPECT image. The tuning of the weight of the MR on the resulting fused image can be performed very quickly, any iterative reconstruction algorithm can be used and, in the case that the SPECT projections are not available, the proposed technique can also be applied directly to the SPECT image, provided that the performance of the scanner is known. The procedure has the potential of increasing the diagnostic value of a SPECT image. Even in the locations of SPECT-MR mismatch it does not significantly affect quantitation over regions of interest (ROIs) whose dimensions are decidedly larger than the SPECT resolution distance. On the other hand, appreciable corrections for partial volume effects are expected in the locations where the contrast in the structural MR matches the corresponding contrast in functional activity.**

***Index Terms*—Functional imaging, image fusion, iterative reconstruction techniques, multimodality imaging, partial volume effect (PVE) correction, single photon emission computed tomography (SPECT) quantitation.**

I. Introduction

THE spatial resolution displayed by brain single photon emission computed tomography (SPECT) images is rather limited, if compared with the one of the corresponding anatomical images (MR or CT images). This lack of resolution generates the so-called partial volume effect (PVE), consisting in an underestimation of a hot spot in a low activity background and, conversely, in an overestimation of a cold spot placed in a hot environment. This fact limits the diagnostic potential of brain SPECT images. For instance, it may be difficult to distinguish between low tracer uptake due to a functional deficit, where brain tissue still exists, from low uptake generated by focal atrophy, where tissue is lost and replaced by cerebrospinal fluid (CSF).

Manuscript received November 12, 2004; revised July 29, 2005. This work was supported in part by MIUR PRIN2002, Inverse Problems in Medical Imaging under Grant 2002013422.

P. Calvini is with INFN, Sezione di Genova, and Dipartimento di Fisica, Università di Genova, I-16146 Genova, Italy.

A. M. Massone is with CNR-INFM LAMIA, I-16146 Genova, Italy (e-mail: massone@ge.infm.it).

F. M. Nobili and G. Rodriguez are with DISEM, Università di Genova, I-16132 Genova, Italy.

Digital Object Identifier 10.1109/TNS.2005.862959

The so-called iterative methods are commonly considered as a valuable tool for obtaining good quality SPECT images where PVEs are corrected to some extent. Unfortunately, the computational burden associated with these techniques is rather high, since at each iteration step a simulation of the data collection process is performed by applying the projection operator A to the current iterate. Such an operator must accurately simulate all the relevant physical factors which influence the acquisition process and, at the software level, it is implemented by means of a suitable routine which must be customized to the specific scanner and to its acquisition configuration. Sometimes the quality of the reconstructions and the obtained amount of PVE correction do not reward adequately for the related management, programming and computational efforts.

Basically, this study proposes an enhancement procedure which fuses a tunable amount of the high-frequency components of the MR image to the SPECT one. When the contrast in the MR image is in the same direction and proportional to the equivalent quantity in the radiotracer map, then, as a side effect, an appreciable correction for PVE is obtained. Indeed, the research upon PVE correction in brain SPECT is a field in full growth, where some systematic strategies have been proposed [1]–[3] and some applications have been published [4], [5], especially in the investigations on the dopaminergic system. However, the procedure presented here is not intended as a new strategy for performing systematic corrections for PVE, since the correctness of its results in terms of PVE compensation is strongly dependent on the contrast match between the structural MR image and the radiotracer uptake distribution. On the other hand, even in the cases of mismatch, the resulting fused images have an added value since they display a synthesis of complementary information from anatomy and function, while retaining the original quantitative content over ROIs sensibly larger than the SPECT resolution distance.

As an example of where the lucky circumstance of contrast match is met throughout most of the brain, we choose the T1-weighted MR images and the corresponding SPECT images of brain blood flow. On the basis of known structure-to-function relationships, the contrast between CSF and the gray matter of the cortex in a T1-weighted MR image is similar to what is expected in a blood flow SPECT image and, for a given patient, the signal gradients are placed in the same locations. Then, the idea is to transfer the high resolution information of the T1-weighted MR to the SPECT image.

In [6] an approach following this strategy has already been proposed and analyzed. There, the enhanced SPECT image is generated by solving a "shifted problem" by means of the conjugate gradient (CG) [7] and the influence of the MR image on

the enhanced reconstruction is tuned by the parameter k. However, that method lacks in flexibility and is computationally demanding since the use of CG is compulsory, the method can be applied only if the SPECT data (the so-called projections) are available and the selection of a suitable value for the parameter k requires to run the iterations for every new value of k.

On the contrary, the method proposed here can be applied with any iterative reconstruction algorithm and it can as well be applied in the case that only the SPECT image is available, provided that the scanner performance is known. Last, the computational burden related to the choice of a suitable value for k is so cheap that it can be performed interactively.

In Section II, the proposed technique is illustrated. An application to patient data can be found in Section III, while in Section IV the way the method affects the corresponding quantitation is analyzed and discussed. In Section V, we present a software phantom study for which true quantitation is known. Conclusions are given in Section VI.

II. Generation of the Improved SPECT Image

The problem of the reconstruction of SPECT data is equivalent to solve the linear system

$$g = Af \tag{1}$$

where the projection matrix A applied to the unknown three-dimensional (3-D) tracer distribution f generates the (known) data g. The ill-conditioned problem stated by (1) may be tackled by using an iterative algorithm and the regularization is usually performed by an early stopping of the iterations (or by means of some equivalent strategy). As long as the choice of the reconstruction algorithm is concerned, the method we propose is more flexible than the one presented in [6], where the use of CG is compulsory. Here, in principle, any iterative algorithm can be chosen and the formulas presented in the following to explain the method can be directly written in a way independent of the particular choice. Thus, we denote by $f_{\rm opt}$ the conventional optimal solution of (1), i.e., the solution which is obtained on the basis of the SPECT data alone and displays a satisfactory tradeoff between noise and resolution. In the specific case of the application presented in the next section, we use the popular Ordered Subset Expectation Maximization (OSEM) algorithm [8], [9] with ten subsets, followed by Gaussian post-filtering [10] (shortly, overiterated and post-filtered OSEM-10).

The method also requires the availability of a recent T1-weighted MR image of the same patient. Such a 3-D image must be accurately coregistered to $f_{\rm opt}$ and properly resampled in order to establish a voxelwise correspondence between the two images. Finally, the voxel values of the MR must be rescaled so that the global activity of the MR equals the equivalent activity present in $f_{\rm opt}$. The volumes over which both activities are evaluated must correspond appreciably. Let us denote by m this coregistered, resampled and normalized version of the MR image. As the next step, the projector A which simulates the performance of the SPECT scanner must be applied to m in order to generate the synthetic projections $g_m = Am$ corresponding to what one collects if a hypothetical MR-like activity distribution is placed in the field of view (FoV) of the scanner. Then, the same reconstruction algorithm with the same parameter(s) [in the case of our computations, OSEM-10 with same iteration number and same full width at half maximum (FWHM) of the Gaussian post-filter] is applied to the new data g_m in order to generate a solution of the linear system

$$g_m = Am. \tag{2}$$

The resulting image $m_{\rm opt}$ represents a sensible estimate of what the conventional tools, i.e., A (the simulator of the scanner performance) and the chosen reconstruction algorithm, would be able to recover, should an activity distribution m be really present in the scanner. Conversely, the difference

$$h = m - m_{\rm opt} \tag{3}$$

represents what those tools would not be able to *see*. According to the strategy of adding to $f_{\rm opt}$ something of what we would have never been able to recover, even if it were really present in the FoV of the scanner, we propose an enhanced version $e_{\rm opt}$ of the SPECT image in terms of the fusion recipe

$$e_{\rm opt} = f_{\rm opt} + kh \tag{4}$$

where k tunes the weight of the MR on the result of the fusion process. Thus, once $f_{\rm opt}$ and h have been obtained at the price of running the chosen reconstruction algorithm twice, the choice of an appropriate value for k can be performed by means of (4), which entails a negligible computational effort. On the basis of some experience, good results are obtained with k taking values of the order of unity. As far as the choice of k is concerned, the method proposed here deeply differs from the one presented in [6], where k was used to rescale m. In fact, there, for every new value of k a new rescaled m was obtained and, then, a new run of CG iterations was required. Moreover, the simple structure of (4) permits simple and accurate analysis of how functional activity in $e_{\rm opt}$ is modified with respect to the original $f_{\rm opt}$, as it will be shown in the next section.

In the above illustrated procedure the SPECT data g are necessary only for the generation of the conventional image $f_{\rm opt}$. Then, if the activity map $f_{\rm opt}$ is already available, but the g data are not, the procedure can be followed anyway starting from the coregistration step. However, the knowledge of the scanner performance is required in order to tune the projector A to the effective acquisition process. Moreover, some info on the reconstruction technique which was used to generate $f_{\rm opt}$ is extremely useful for performing a good choice of the reconstruction algorithm to be applied to the g_m data.

We conclude this section with the remark that a 3-D version of the Frequency Encoding (FE) algorithm [11] would be able to halve the computational cost of the proposed technique. In fact, an application of a 3-D version of FE permits to generate $m_{\rm opt}$ simply by blurring m with a Gaussian kernel of suitable FWHM. Once $m_{\rm opt}$ has been obtained in this very cheap way, the remaining steps can be performed. However, the FE-based algorithm is suboptimal, its main drawback being that no optimal FWHM exists that mimics satisfactorily the whole procedure of synthetic data generation and reconstruction to obtain

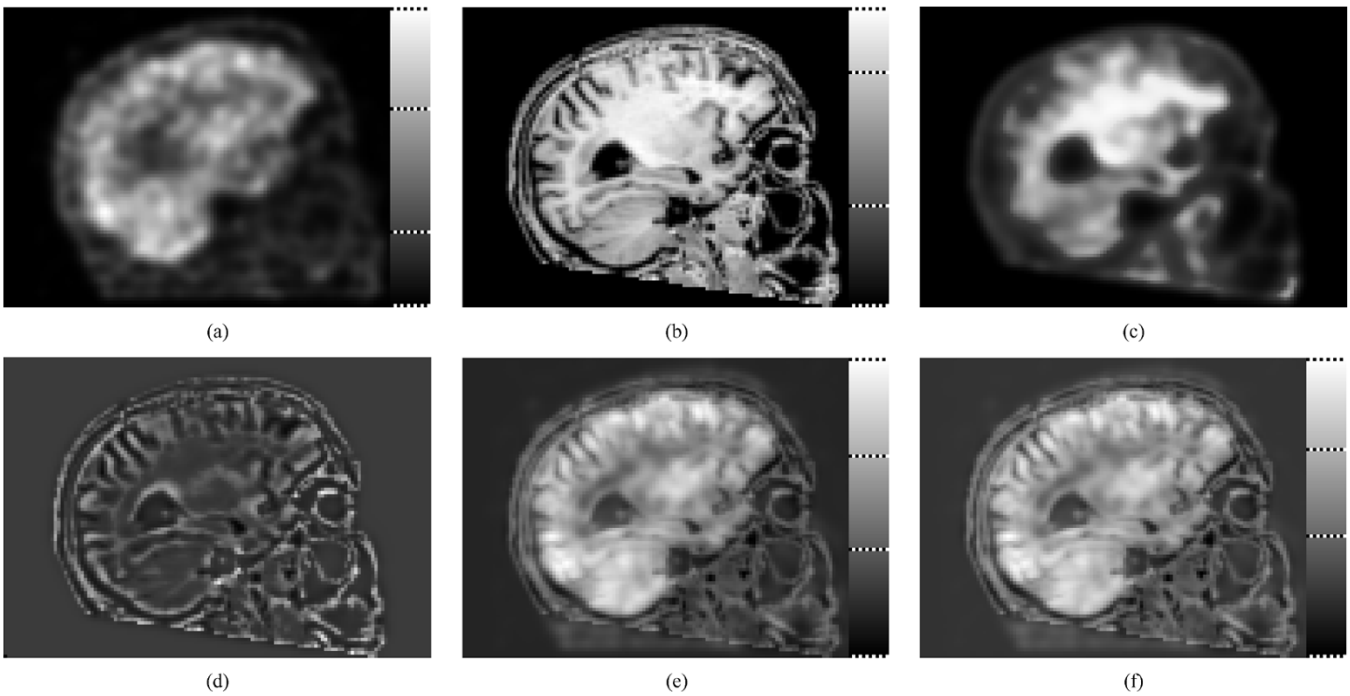

Fig. 1. The same sagittal slice cut from different images of the same patient. (a) Conventional reconstruction $f_{\rm opt}$ obtained as iterate 12 of OSEM-10 with Gaussian post-filtering (FWHM $= 8$ mm). From top to bottom the gray level color bar gives the relative intensity range for gray matter, white matter and CSF/background. (b) T1-weighted MR image m coregistered to $f_{\rm opt}$. Color bar from top to bottom: white matter, gray matter and CSF/background/fat. (c) $m_{\rm opt}$, the *visible* part of m. (d) h, the *invisible* part of m. (e) Enhanced SPECT image with $k = 0.9$. (f) Same with $k = 1.2$. Color bars in (e) and (f) follow the gray level sequence as in (a) (see text).

$m_{\rm opt}$. An evidence for this comes from the results of the simulation study presented in Section V. Such results show that the spatial resolution displayed by the reconstructions of a phantom are strongly depth-dependent. Such an effect cannot be successfully mimicked by any space-invariant blur.

III. Application of the Proposed Method

Here the results are presented of an application of the proposed method to patient data relative to a blood flow scan. In this case a contrast match is expected between the functional map and the T1-weighted MR image over relevant portions of the brain volume. Therefore, PVE corrections of significant amount are expected (and really found) in the sites of contrast match.

The SPECT data were acquired with a *GE Millennium VG* two-headed scanner equipped with LEHR parallel beam collimators. SPECT acquisition started 60 min after the i.v. injection of 1 000 MBq of $^{99\,\rm m}$Tc-N,N"-1,2-ethylene diylbis-L-cysteine diethyl ester dihydrochloride (ECD; Neurolite Bristol-Myers Squibb, USA), according to the guidelines of the European Society of Nuclear Medicine [12]. A step-and-shoot acquisition with a radius of rotation of 14 cm produced 120 projections evenly spaced over 360°, with the collection of 9 600 000 total counts. The pixel size of the acquisition matrix is 2.9 mm, thanks to an electronic zoom applied in the data collection phase (zoom factor $\cong$ 1.5). The projector A simulating the scanner acquisition accounts for the collimator blur and photon attenuation. No compensation for scatter is performed. The 2-D+1 approximation [13] is applied to the simulation of space-variant collimator blur, while photon attenuation is modeled with the approximation of a linear coefficient uniform inside the skull and equal to 0.11 cm^{-1}. Such a value for the attenuation coefficient is used following a common practice which aims at avoiding attenuation overcompensation due to scatter (the standard value relative to water at the 140 keV energy of $^{99\,\rm m}$Tc is 0.15 cm^{-1}). In the reconstruction phase also a digital zoom is applied in order to generate SPECT images sampled by cubic voxels with 2-mm sides. This is done in order to prevent an excessive loss in spatial resolution of the MR image after its coregistration to the SPECT image $f_{\rm opt}$.

As already anticipated, the selected reconstruction algorithm is overiterated OSEM-10 followed by post-filtering: $f_{\rm opt}$ is obtained by applying a Gaussian filter with FWHM $= 8$ mm to iterate 12. In Fig. 1(a) a sagittal section cut from $f_{\rm opt}$ is shown.

The T1-weighted MR image of the same patient was acquired with a 1.5-T Gyroscan system (Philips Medical Systems). The resulting image, sampled by cubic voxels whose side is about 1 mm, is coregistered to $f_{\rm opt}$, resampled in voxelwise correspondence with $f_{\rm opt}$ (voxels with 2-mm side) and normalized so that its activity equals the one of $f_{\rm opt}$. The MR image is thresholded by zeroing fat activity and, in general, all activity higher than that of white matter. The image obtained by this simple operation has a more SPECT-like aspect than the original one. In Fig. 1(b) a sagittal section cut from m is shown, which, thanks to the coregistration, corresponds to the section shown in Fig. 1(a). From top to bottom the gray level bar in Fig. 1(a) suggests the relative intensity range for gray matter, white matter and CSF/background. On the contrary, the order for Fig. 1(b) is white matter, gray matter and CSF/background/fat.

Then, the projector A is applied to m to produce the synthetic data g_m, which are subsequently reconstructed by 12 iterations of OSEM-10 followed by Gaussian post-filtering (same FWHM

as before). In this way the estimate $m_{\rm opt}$ is obtained and subtracted from m, according to (3), to generate h, the *invisible* part of m. In Fig. 1(c) a sagittal section cut from $m_{\rm opt}$ is shown, while in Fig. 1(d) the corresponding section of h is shown.

Finally, enhanced SPECT images can be obtained by using (4) with different values of k. We obtain an appreciable improvement in the quality of the image for values of k ranging from 0.6 to 1.2. For values of k sensibly higher than unity the quality of the enhanced image worsens because of the presence of excessive contrast and negative voxel values. In Fig. 1(e) and (f) the same sagittal section is shown, produced with values of k equal to 0.9 and 1.2, respectively. In these figures, the gray level sequence shown by the intensity bars is the same as in Fig. 1(a).

The way the proposed technique modifies the activity distribution of $f_{\rm opt}$ can be inspected by means of plots of voxels values along a selected line in the images. In the sections shown in Fig. 1, a horizontal line is drawn which crosses the lateral ventricle, just above the hippocampal formation, at the same height in all figures. Thanks to the coregistration, the voxel positions along such a line are in geometrical (and anatomical) correspondence in all images. In Fig. 2(a), the plot is shown of the voxel values relative to the conventional $f_{\rm opt}$. The activity in the ventricle (center at 45) is overestimated because of PVE, which also affects the "shape" of the ventricle. On the basis of an inspection of the MR, a null uptake region spanning about ten voxels (i.e., from voxel 40 to voxel 50) is expected, since the uptake of the CSF filling the ventricle is supposed to be negligible in virtue of pharmacokinetic considerations. In Fig. 2(b), the voxel values are plotted along the same line in h, the high-frequency part of m. The boundaries of the ventricle can be easily identified in h, the *invisible* image. This implies that the conventional tools of functional imaging are unable to locate such boundaries with the accuracy supplied by the MR. Last, in Fig. 2(c), the plot is shown of the voxel values in the enhanced images, with $k = 0.9$ (continuous line) and $k = 1.2$ (dashed line; the profile of $f_{\rm opt}$ is also superimposed as a dotted line for comparison). In Fig. 2(c), the position and boundaries of the lateral ventricle can be easily identified and a nearly flat region of low uptake is displayed. Of course, with increasing values of k the "hole" representing the ventricle activity deepens more and more, ultimately with voxel values taking negative values not only in the ventricle, but also in other places in the whole volume spanned by the enhanced SPECT image. The appearance of such pathologies in the activity map suggests an upper bound for the appropriate values of k.

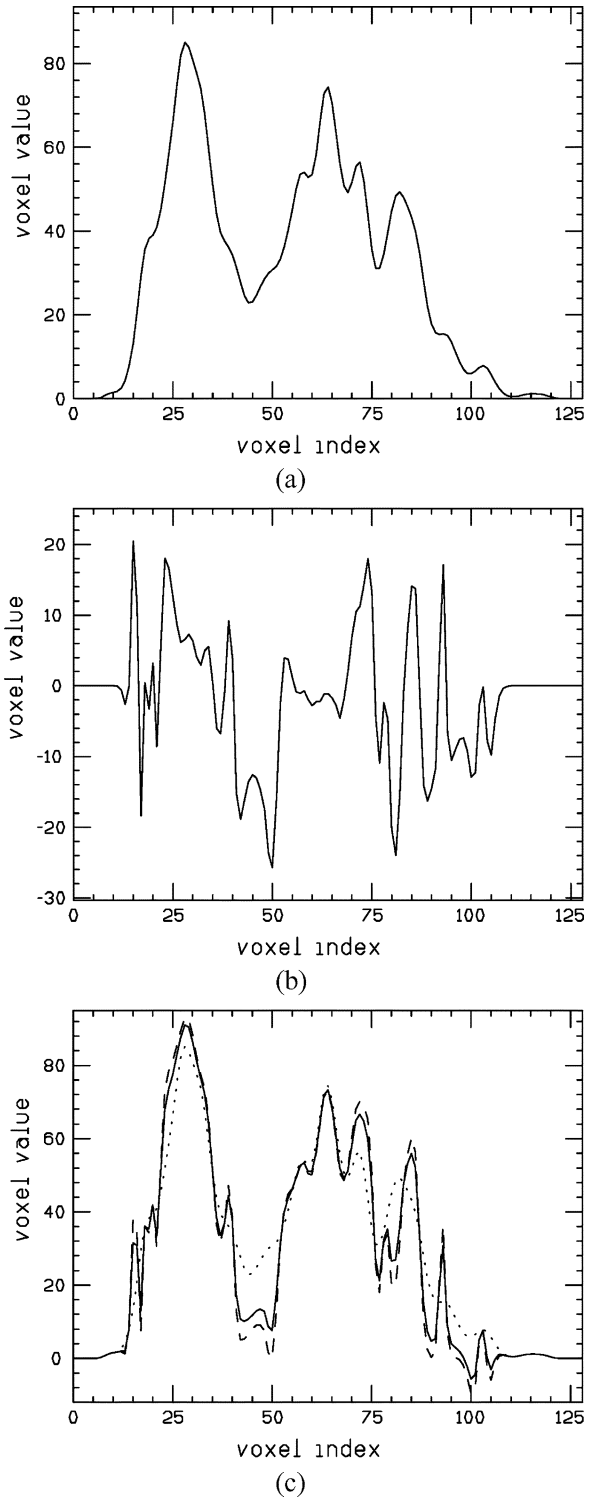

Fig. 2. Plot of the voxel values along a horizontal line. (a) Fig. 1(a) (conventional SPECT activity $f_{\rm opt}$). (b) Fig. 1(d) (h, the *invisible* part of m). (c) Fig. 1(e), (enhanced image with $k = 0.9$; continuous line) and Fig. 1(f) (enhanced image with $k = 1.2$, dashed line); the plot of Fig. 2(a) is also drawn for comparison (dotted line).

IV. Quantitative Content of the Enhanced Images

In the previous sections, a fusion technique which generates enhanced SPECT images is illustrated and applied to a patient case. Here, on the basis of the images relative to that case, the effects on quantitation of the proposed fusion process are estimated and discussed.

The counts c_f relative to an ROI specified by the binary map χ and drawn on the image $f_{\rm opt}$ can be evaluated as the dot product between χ and $f_{\rm opt}$ as follows:

$$c_f = \sum_i \chi_i (f_{\rm opt})_i \,. \tag{5}$$

Here voxels are labeled by a single index on the basis of lexicographic ordering and, thus, χ_i represents the value of the ith voxel of χ. It equals unity if the voxel belongs to the ROI and vanishes if it does not. Analogously, the counts c_e (or c_h) contained in the same ROI drawn on $e_{\rm opt}$ (or on h) can be evaluated

by means of a formula equivalent to (5), where $e_{\rm opt}$ (or h) replaces $f_{\rm opt}$. The present analysis aims at giving estimates, for various kinds of ROIs, of the percent deviation in count evaluation (PDCE)

$$\text{PDCE} = 100\frac{|c_e - c_f|}{c_f} \tag{6}$$

between $f_{\rm opt}$ and $e_{\rm opt}$. It will be shown that PDCE is a function of k, of the ROI size and of the ROI content. Since PDCE displays instability for too low values of c_f, only the ROIs will be considered for which the corresponding c_f's obey the following requirement:

$$c_f \geq 0.08\, v_{\max} \sum_i \chi_i \tag{7}$$

where $v_{\max}$ is the maximum voxel value present in $f_{\rm opt}$. The sum in (7) gives the number of voxels belonging to the ROI defined by χ. The ROIs which are discarded by this criterion essentially belong to the background and are consequently void of any clinical interest.

As concerns the effects produced by changing k, an inspection of (4), (5), and (6) shows that PDCE has a linear dependence on k according to

$$\text{PDCE} = 100\, k\frac{|c_h|}{c_f} \tag{8}$$

where $k = |k|$ since $k \geq 0$. On the basis of this result all the following computations are performed with an enhanced image $e_{\rm opt}$ produced with $k = 1$ and all the PDCE estimates proposed here correspond to such a choice. It must be recalled that the PDCE values scale linearly with k if this parameter takes values different from unity.

We now turn to investigate how PDCE depends on the kind of ROI. Following the empirical technique already used in [6], we use cubic ROIs of side L ranging from 2 mm (the voxel size) to 40 mm. The latter length approximately corresponds to three times the estimated resolution distance in $f_{\rm opt}$. In the $128 \cdot 128 \cdot 90$ voxel volumes of $f_{\rm opt}, h$ and $e_{\rm opt}$ all possible cubic ROIs are located by suitable software and the populations of the corresponding counts are generated. The analysis consists in evaluating average values and in recording maximum values of $|c_h|$ and $|c_e - c_f|/c_f$ for every class consisting of all the ROIs having the same side L. The ROIs placed in the locations yielding c_f values which do not meet requirement (7) are discarded.

It can be shown that the complex recipe for generating image h is grossly equivalent to applying a high-pass filter to m. Thus, h contains only high spatial frequencies and this is confirmed by the fact that in h the sum of all counts as well as the sum of the counts contained in ROIs encompassing relevant portions of its volume vanish. For smaller ROIs this is not true. This fact suggests that the fusion process realized by (4) does not really add foreign counts to $f_{\rm opt}$, but simply moves functional activity from one location to another. The distance over which counts are displaced is suggested by the size of the ROIs in h containing count values which are so high as to sensibly modify the corresponding c_f values in the same ROIs. On the basis of these considerations we introduce the normalized activity for an ROI in h (NAh)

$$\text{NAh} = \frac{|c_h|}{v_{\max}\sum_i \chi_i} \tag{9}$$

as a measure of the "contaminating" potential of h on $f_{\rm opt}$ in that ROI. The denominator in (9) is the same for all the ROIs with the same L and represents the reference value for ROI counts in $f_{\rm opt}$, given as the product of $v_{\max}$ times the number of voxels. In Fig. 3(a) for each value of L, the average value (continuous line) and the maximum recorded value (dashed line) of NAh are plotted. The average and maximum values of NAh approach zero with increasing L, thus supporting the previous considerations on the properties of h. For $L = 14$ mm, a length comparable with the SPECT resolution distance, the average value of NAh is 0.007 while the maximum is about 0.08. If the average value is considered, the conclusion is drawn that for 14-mm ROIs the enhancement procedure modifies by about 0.9% the counts in gray matter ROIs, where the average voxel value may be $0.8\, v_{\max}$ and by about 9% the counts in CSF ROIs, where the average voxel value is about $0.08\, v_{\max}$. If, more pessimistically, the maximum value is considered, the conclusion is drawn that for 14-mm ROIs the enhancement procedure modifies at most by 10% the counts in gray matter ROIs and by 100% the counts in CSF ROIs.

The latter considerations suggest that PDCE depends not only on the ROI side L, but also on the ROI content. Thus, each count population associated to a fixed value of L is divided further on into three subclasses, namely gray matter ROIs (average voxel values between $0.65\, v_{\max}$ and $v_{\max}$), white matter ROIs (average voxel values between $0.24\, v_{\max}$ and $0.65\, v_{\max}$) and, last, CSF or background ROIs (average voxel values between $0.08\, v_{\max}$ and $0.24\, v_{\max}$). The analysis performed upon these subclasses generates three sets of average values and three sets of maximum values for PDCE in function of L. In Fig. 3(b) the PDCE averages relative to gray matter ROIs (dashed line), white matter ROIs (continuous line) and CSF or background ROIs (dot-and-dash line) are plotted in function of L. In Fig. 3(c) the PDCE maximum values relative to gray matter ROIs (dashed line), white matter ROIs (continuous line) and CSF or background ROIs (dot-and-dash line) are plotted in function of L. If 1% is chosen as a threshold for PDCE average values, by inspection of Fig. 3(b) the ROI sides $L = 11$ mm, 20 mm, and 34 mm are obtained, respectively, for gray matter, white matter, and CSF ROIs. If 10% is chosen as a threshold for PDCE maximum values, by inspection of Fig. 3(c) the ROI sides $L = 8$ mm, 22 mm, and 32 mm are obtained, respectively, for gray matter, white matter, and CSF ROIs. Thus, the present analysis indicates that the proposed fusion technique does not appreciably modify high functional activity. On the other hand, functional activity of intermediate or low intensity may be displaced by two or even three SPECT resolution lengths. The lower is the intensity, the higher is the probability of a relevant displacement. However, as already discussed in [6], such displacements of functional activity must not always be considered as harmful effects, since in some occasions they might well be the symptom of a resolution gain. An example of such a possibility has been proposed in the last part of the previous section (see Fig. 2). In general,

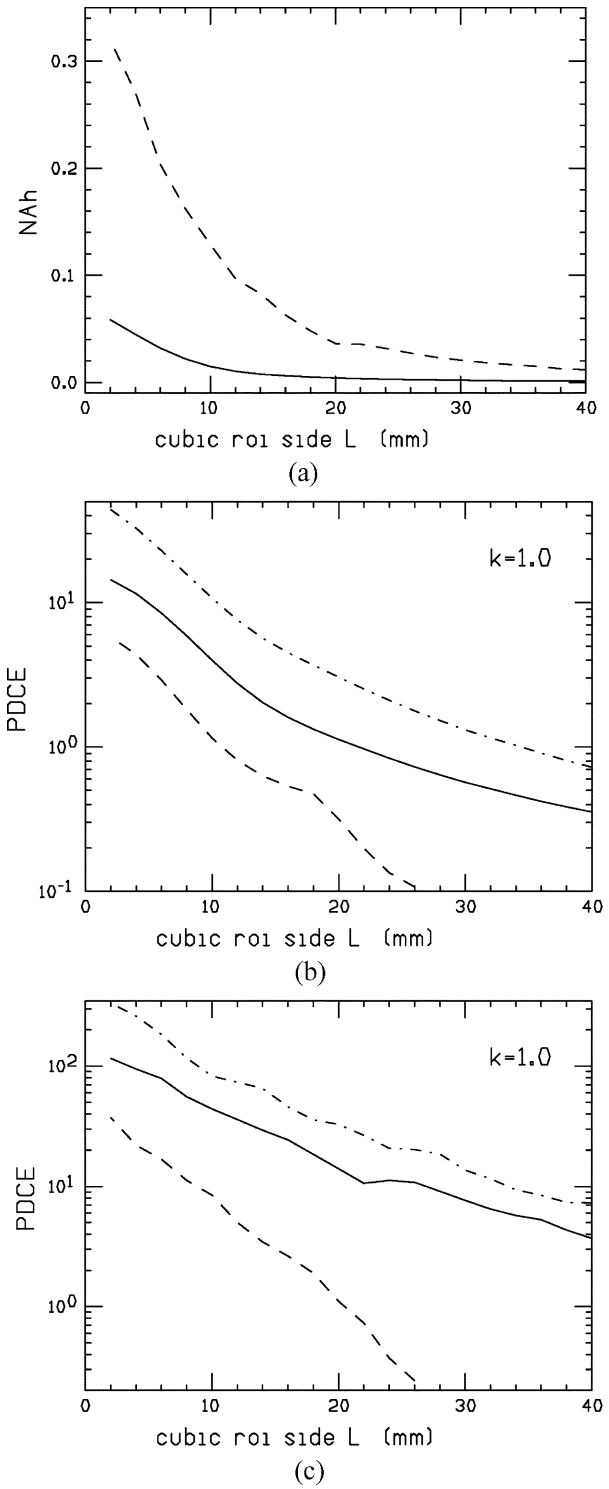

Fig. 3. (a) Plot of NAh in function of cubic ROI side L [NAh is defined in (9)]: average value (continuous line) and maximum recorded value (dashed line) over the population of all cubic ROIs which can be located in h. (b) Plots in function of cubic ROI side L of PDCE average values (PDCE is defined in (6)): average values over gray matter ROIs (dashed line), over white matter ROIs (continuous line) and over low count ROIs (dot-and-dash line). (c) Plots in function of cubic ROI side L of PDCE maximum recorded values: maximum values over gray matter ROIs (dashed line), over white matter ROIs (continuous line) and over low count ROIs (dot-and-dash line).

this favorable situation occurs when the MR contrast matches the equivalent contrast in the functional image, as it typically occurs in correspondence of the CSF-gray matter boundary for the T1-weighted MR images. Of course, also situations of mismatch occur unavoidably and, thus, the interpretation of the enhanced images may require the expertise of a skilled SPECT reader.

V. Resolution Phantom Study

In order to evaluate to what extent the proposed method affects the activity of a conventional SPECT image in a variety of match/mismatch situations, we also present the results from a numerical simulation based on the Jaszczak resolution phantom. A software version of the phantom was preferred to a physical one because it permits a more flexible approach. In this study a SPECT activity distribution and a structural template are generated with some kind of known mismatch between each other with the purpose of testing the performance of our fusion technique when it is fed with good info and also when it is deceived.

A real Jaszczak phantom underwent an MR scan (hot rods filled with copper sulphate), yielding a stack of high resolution slices, sampled by 512×512 pixels (pixel side $=$ 0.59 mm). Then, a single two-dimensional (2-D) slice was chosen from the stack. It was downsampled to obtain an image sampled by 128×128 pixels (pixel\ side$\cong$ 2.2 mm), in conformity with image size and sampling rate usually adopted in SPECT imaging. The 3-D software phantom was obtained by stacking 45 copies of the so-obtained 2-D image, simulating in this way a 10–cm-thick cylindrical slab of lucite drilled with the characteristic pattern of holes. The central section (section number 23) of the phantom is shown in Fig. 4(a), where the six sectors are labeled with Roman numerals for easier reference. From sector I to VI, the rod diameters are 12.4, 10.6, 8.8, 7.1, 5.3, and 3.5 mm (estimated from the original high-resolution 512×512 MR image). Photon attenuation is modeled in terms of a linear coefficient uniform inside the cylinder containing the set of holes and equal to 0.16 cm^{-1}, a value compatible with lucite. The trace of the boundary of the attenuating cylinder is shown in Fig. 4(a) by the dotted circle and its diameter was derived from the MR scan to be 205 mm.

From the 3-D hot rod phantom, two different activity distributions were generated by adopting the technique of zeroing activity inside some spherical ROIs. This strategy of using spherical ROIs allows for 3-D effects in an axially invariant phantom. All ROIs have their centers in slice 23 and their radii, in order from sector I to VI, take the values 12.6, 11.0, 9.7, 8.2, 6.6, and 4.4 mm. Such values have been chosen as slightly less than half the distance between the axes of two neighboring rods, thus there is no overlap between two possibly adjacent ROIs. Then, the simulated functional activity distribution, denoted by f, was prepared by selecting two ROIs in each sector, one deeply placed inside the phantom and the other one in an external position. The central section of f is shown in Fig. 4(b), where the small dots indicate the centers of the ROIs where activity was zeroed with respect to the original phantom. The total activity in f was scaled in order to generate a 2.8-Mcount data set g when projector A, which also models attenuation, is applied to it. Should attenuation be neglected, the same activity distribution would generate an 8-Mcount data set.

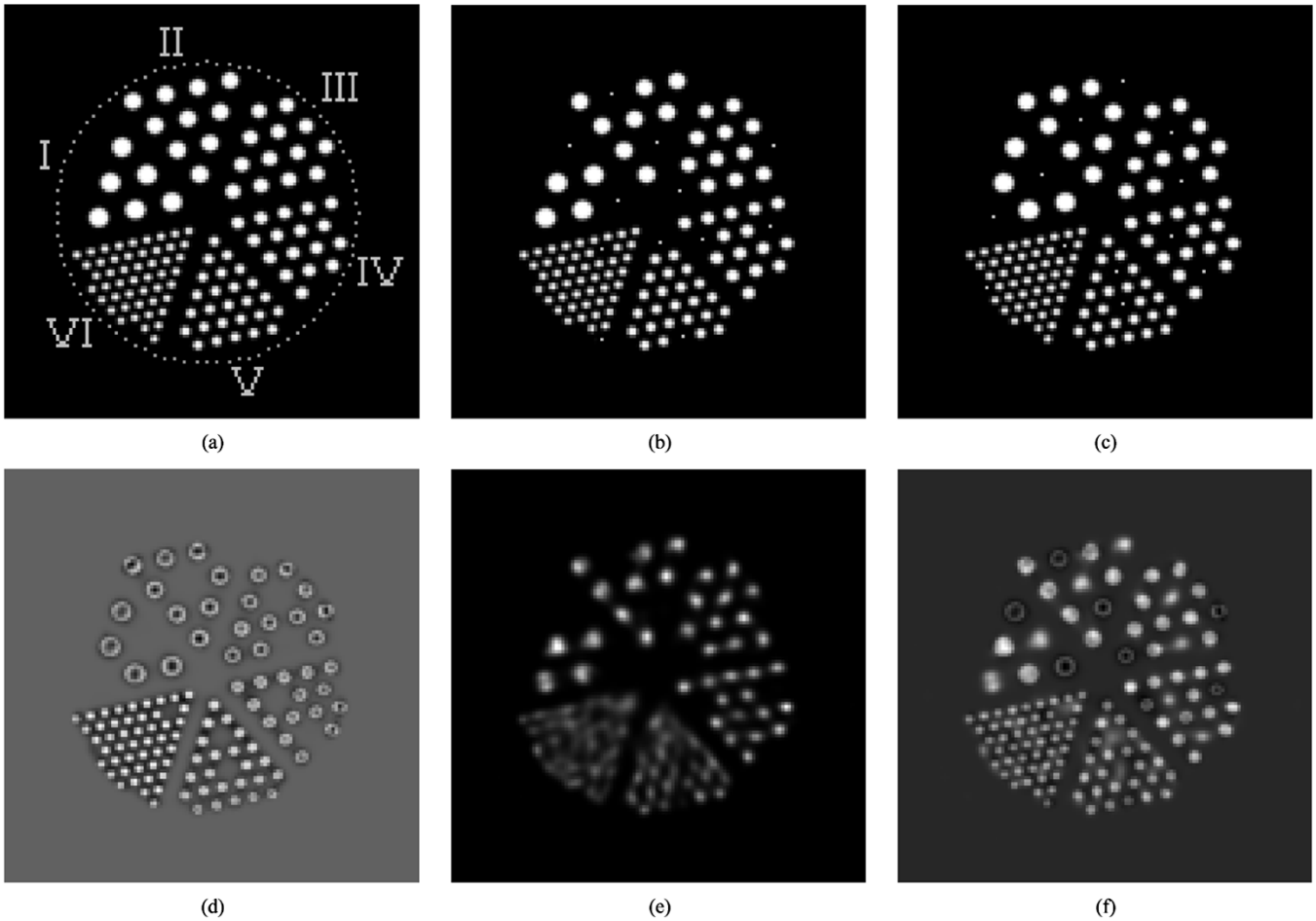

Fig. 4. (a) Central slice cut from a software version of the Jaszczak resolution phantom. Uniform attenuation is assumed inside a cylinder whose boundary is shown in this slice by the dotted circle. The six sectors of the phantom are labeled by Roman numerals. (b) Corresponding slice of f, the assumed functional activity map used to generate the synthetic SPECT data. (c) Corresponding slice of m, the assumed structural template. In (b) and (c) the dots indicate the centers of the spherical ROIs where functional (b) or structural (c) signal was zeroed. (d) Central slice of h, the *invisible* part of m. (e) Corresponding slice of $f_{\rm opt}$, the conventional reconstruction of the synthetic SPECT data obtained with 22 iterations of OSEM-15 followed by Gaussian post-filtering (FWHM $=$ 6 mm). (f) Corresponding slice of the enhanced SPECT image with $k = 0.8$ (see text).

The structural template m was derived from the original phantom by zeroing structural signal inside two spherical ROIs in each sector. No ROI in m coincides with an ROI defined in the functional f. From sector I to IV, the criterion was used to take one ROI on the line connecting the pair of ROIs of vanishing activity in f and a second ROI far apart. In sectors V and VI, the ROIs were taken randomly. The central section of the structural template is shown in Fig. 4(c), where the small dots indicate the centers of the ROIs where the signal was zeroed with respect to the original phantom.

The functional data g were contaminated with Poisson noise and reconstructed with OSEM-15. It was found that 22 iterations followed by Gaussian post-filtering with an FWHM $=$ 6 mm generated $f_{\rm opt}$. The optimization criterion was the minimization of the normalized root-mean-square error (NRMSE) of the reconstruction with respect to f. The minimum NRMSE value was 52%. The central section of $f_{\rm opt}$ is shown in Fig. 4(e), where it can be noticed that the spatial resolution in the reconstruction is depth dependent. The effect is particularly remarkable in sectors V and VI, where some external rods can still be distinguished while deeply placed rods are not resolved.

Then, new synthetic data were generated by applying projector A to the structural template m and subsequently reconstructed with OSEM-15 to produce $m_{\rm opt}$ (same iteration number and same FWHM as in the recovery of the functional data). Last, the high-frequency image h was obtained by means of (3) and the enhanced reconstruction $e_{\rm opt}$ was obtained from (4) with $k = 0.8$. The central sections of h and $e_{\rm opt}$ are shown, respectively, in Fig. 4(d) and (f). The criterion of minimizing the NRMSE was not applied for making the choice $k = 0.8$, since this strategy gives $k \cong 1$ and the corresponding enhanced image suffers from too negative values in the locations where f vanishes, but m does not. A better approach is to find the value for k which gives an enhanced image with minimal background activity in absolute value. By taking advantage of the fact that in a simulation the truth is known, we are able to specify the background ROI in f as the set of all vanishing voxels. Since f and all its reconstructions are in geometrical correspondence, the same ROI can as well be used for evaluating background activity in $f_{\rm opt}$ and in any $e_{\rm opt}$. Thus, in the case of $f_{\rm opt}$ one gets a value which is 11.7% of all counts found in $f_{\rm opt}$. This represents an estimate of PVE. As long as $f_{\rm opt}$ is concerned,

TABLE I
QUANTITATION IN ROIS WHERE $f = 0$ AND $m \neq 0$. (COUNTS IN COLUMN 3 ARE THE ORIGINAL ONES BEFORE BEING ZEROED)

ROI in sector	voxels in ROI	counts in ROI	expected (%)	f_{opt} (%)	e_{opt} (%)	e_{opt}–f_{opt} (%)
I (outer)	782	372	0.0	2.6	4.7	2.1
I (inner)	782	377	0.0	3.2	7.3	4.1
II (outer)	524	237	0.0	4.3	7.0	2.7
II (inner)	506	241	0.0	6.8	13.2	6.4
III (outer)	356	169	0.0	10.0	14.7	4.7
III (inner)	368	172	0.0	9.2	14.5	5.3
IV (outer)	203	94	0.0	9.3	13.9	4.6
IV (inner)	228	98	0.0	7.1	19.1	12.0
V (outer)	112	42	0.0	25.9	34.4	8.5
V (inner)	106	46	0.0	33.2	55.3	22.1
VI (outer)	33	17	0.0	25.6	45.1	19.5
VI (inner)	42	21	0.0	36.0	60.2	24.2

there is no distinction between activity and activity in absolute value, since $f_{\rm opt}$ is a nonnegative image. On the contrary, an enhanced image may have negative voxels and the distinction is important. The value $k = 0.8$ is selected as the one which generates the $e_{\rm opt}$ with minimal background activity in absolute value. The minimum obtained is 6.3%. Once the optimal value for k is found, one can as well evaluate background activity in $e_{\rm opt}$ by taking signs into account. The result is 3.4%. Then, the conclusion can be drawn that our method is able to reduce global PVE in the phantom background from 11.7% to 3.4%.

An inspection of Fig. 4 permits some qualitative considerations on $e_{\rm opt}$ compared with $f_{\rm opt}$. In the locations where m matches f the improvement of $e_{\rm opt}$ over $f_{\rm opt}$ is evident. In the locations of mismatch the behavior of $e_{\rm opt}$ can be explained in terms of (4). In the ROIs where $f \neq 0$ and $m = 0$, $e_{\rm opt}$ is very similar to $f_{\rm opt}$ since there h practically vanishes. On the other hand, in the ROIs where $f = 0$ and $m \neq 0$, $e_{\rm opt}$ is very similar to h since there it is $f_{\rm opt}$ that practically vanishes. The larger are the ROIs, the truer are the above assertions. From the point of view of the SPECT reader, the latter situation (structural signal present with weak or vanishing functional activity) is the one which deserves some care.

We conclude this section by showing quantitative results in ROI counts relative to the match/mismatch situations created in this simulation study. In Table I, quantitation results are shown relative to the ROIs where functional activity is missing in the presence of (wrong) structural signal. The percentages presented in columns 4–7 have been evaluated with respect to the ROI counts of column 3. Such counts represent the original ROI counts, obviously before being zeroed. An inspection to the results in Table I indicates that the proposed method, fed with wrong information, systematically overestimates activity with respect to $f_{\rm opt}$ and that the error increases where the SPECT resolution worsens, i.e., if we commute from outer to inner ROIs or we move toward sectors with very small ROIs. However, the error of the proposed method is tolerable for ROIs whose dimensions are larger than or comparable with the SPECT resolution distance (thus, from sector I to IV). In Table II, quantitative results are shown relative to the ROIs where functional activity is present in the absence of structural info. In such a situation, our method is simply inactive and gives results quite comparable with the ones of the conventional reconstruction method. The results seem independent of the ROI position with respect to other mismatch spots. Some appreciable inaccuracy occurs only in sector VI. Last, in Table III, the quantitative gain in accuracy is presented relative to the ROIs where our method is fed with good info. Here the method is able to efficiently compensate at all distance scales for the informational void (if any) which is left by the conventional reconstruction technique.

TABLE II
QUANTITATION IN ROIS WHERE $f \neq 0$ AND $m = 0$

ROI in sector	voxels in ROI	counts in ROI	expected (%)	f_{opt} (%)	e_{opt} (%)	e_{opt}–f_{opt} (%)
I (betw)	804	382	100.0	94.3	91.0	-3.3
I (far)	768	374	100.0	97.2	94.9	-2.3
II (betw)	485	240	100.0	91.7	88.6	-3.1
II (far)	485	229	100.0	95.7	93.6	-2.1
III (betw)	361	166	100.0	84.0	79.2	-4.8
III (far)	356	164	100.0	90.5	83.3	-7.2
IV (betw)	219	98	100.0	77.1	74.4	-2.7
IV (far)	206	100	100.0	87.8	82.8	-5.0
V (rand)	112	46	100.0	76.7	76.6	-0.1
V (rand)	112	46	100.0	98.9	96.4	-2.5
VI (rand)	36	15	100.0	96.9	71.3	-25.6
VI (rand)	36	16	100.0	86.0	56.3	-29.7

TABLE III
QUANTITATION IN ROIS WHERE $f \neq 0$ AND $m \neq 0$

ROI in sector	voxels in ROI	counts in ROI	expected (%)	f_{opt} (%)	e_{opt} (%)	e_{opt}–f_{opt} (%)
I	751	372	100.0	94.0	98.7	4.7
II	524	235	100.0	98.2	101.0	2.8
III	362	173	100.0	91.5	99.2	7.7
IV	215	96	100.0	89.1	97.4	8.3
V	112	43	100.0	86.3	95.4	9.1
VI	36	17	100.0	50.5	82.2	31.7

VI. CONCLUSION

A flexible method is proposed which has the potential of improving the diagnostic potential of a patient's SPECT image on the basis of the structural info derived from the T1-weighted MR image of the same subject. Such an enhancement procedure introduces anatomical features into the SPECT image through slight displacements of the original activity distribution, without adding any extra counts. The magnitude of such displacements depends on the amount of functional activity to be moved and even in the most "dangerous" cases, it is always comparable with the original SPECT resolution distance. High functional activity is never displaced appreciably, whereas intermediate or low activity may be displaced to some extent. Quantitation over ROIs whose dimensions are decidedly larger than the SPECT resolution distance is not affected sensibly. Moreover, the analysis presented at the end of Section III in the case of patient data and the results of the numerical simulation of Section V indicate that in the locations where the MR contrast matches the

expected contrast of the SPECT activity distribution, there the improvement in spatial resolution and the consequent correction for PVE are appreciable.

ACKNOWLEDGMENT

The authors wish to thank Prof. M. Bertero from the Dipartimento di Informatica e Scienze dell'Informazione for stimulating discussions and helpful criticism.

REFERENCES

[1] O. G. Rousset, Y. Ma, and A. C. Evans, "Correction for partial volume effects in PET: Principle and validation," *J. Nucl. Med.*, vol. 39, no. 5, pp. 904–911, May 1998.

[2] M. Koole, R. Van de Walle, K. Van Laere, Y. D'Asseler, S. Vandenberghe, I. Lemahieu, and R. A. Dierckx, "Study of the quantification of FBP SPECT images with a correction for partial volume effects," *IEEE Trans. Nucl. Sci.*, vol. 49, no. 1, pp. 69–73, Feb. 2002.

[3] Y. Du, B. M. W. Tsui, and E. C. Frey, "Partial volume effect compensation for quantitative brain SPECT imaging," *IEEE Trans. Med. Imag.*, vol. 24, no. 8, pp. 969–976, Aug. 2005.

[4] M. Koole, K. Van Laere, R. Van de Walle, S. Vandenberghe, L. Bouwens, I. Lemahieu, and R. A. Dierckx, "MRI guided segmentation and quantification of SPECT images of the basal ganglia: A phantom study," *Comput. Med. Imaging Graph.*, vol. 25, no. 2, pp. 165–172, Mar. 2001.

[5] M. Soret, P. M. Koulibaly, J. Darcourt, S. Hapdey, and I. Buvat, "Quantitative accuracy of dopaminergic neurotransmission imaging with ^{123}I SPECT," *J. Nucl. Med.*, vol. 44, no. 7, pp. 1184–1193, Jul. 2003.

[6] P. Calvini, P. Vitali, F. Nobili, and G. Rodriguez, "Enhancement of SPECT reconstructions by means of coregistered MR data," *IEEE Trans. Nucl. Sci.*, vol. 48, no. 3, pp. 750–755, Jun. 2001.

[7] R. H. Huesman, G. T. Gullberg, W. L. Greenberg, and T. F. Budinger, "Donner algorithms for reconstruction tomography," in *RECLBL Library Users' Manual*. Berkeley, CA: Lawrence Berkeley Lab., Univ. California, Oct. 1977.

[8] H. M. Hudson and R. S. Larkin, "Accelerated image reconstruction using ordered subsets of projection data," *IEEE Trans. Med. Imag.*, vol. 13, no. 4, pp. 601–609, Dec. 1994.

[9] J. Li, R. J. Jaszczak, K. L. Greer, and R. E. Coleman, "Implementation of an accelerated iterative algorithm for cone-beam SPECT," *Phys. Med. Biol.*, vol. 39, no. 3, pp. 643–653, Mar. 1994.

[10] F. J. Beekman, E. T. P. Slijpen, and W. J. Niessen, "Selection of task-dependent diffusion filters for the post-processing of SPECT images," *Phys. Med. Biol.*, vol. 43, no. 6, pp. 1713–1730, Jun. 1998.

[11] M. Quarantelli, B. Alfano, M. Larobina, E. Tedeschi, A. Brunetti, E. M. Covelli, A. Ciarmiello, C. Mainolfi, and M. Salvatore, "Frequency encoding for simultaneous display of multimodality images," *J. Nucl. Med.*, vol. 40, no. 3, pp. 442–447, Mar. 1999.

[12] K. Tatsch, S. Asenbaum, P. Bartenstein, A. Catafau, C. Halldin, L. S. Pilowsky, and A. Pupi, "European association of nuclear medicine procedure guidelines for brain perfusion SPET using $^{99\,m}$Tc-labeled radiopharmaceuticals," *Eur. J. Nucl. Med. Mol. Imaging*, vol. 29, no. BP36-42, Oct. 2002.

[13] P. Boccacci, P. Bonetto, P. Calvini, and A. R. Formiconi, "A simple model for the efficient correction of collimator blur in 3-D SPECT imaging," *Inverse Problems*, vol. 15, no. 4, pp. 907–930, Aug. 1999.